

Reflection of linear internal tides from realistic topography: The Tasman continental slope

JODY M. KLYMAK, *

School of Earth and Ocean Sciences and Department of Physics and Astronomy, University of Victoria, Victoria, Canada

Harper L. Simmons and Dmitry Braznikov

University of Alaska Fairbanks, Fairbanks, Alaska, USA

Samuel Kelly

Large Lakes Observatory and Department of Physics, University of Minnesota Duluth, Duluth, Minnesota

Jennifer A. MacKinnon, Matthew H. Alford, and Robert Pinkel

Scripps Institution of Oceanography, University of California, San Diego, La Jolla, California

Jonathan D. Nash

College of Ocean and Atmospheric Science, Oregon State University, Corvallis, Oregon

* Corresponding author address: Jody Klymak, University of Victoria, Victoria, BC, Canada

E-mail: jklymak@uvic.ca

ABSTRACT

9 The reflection of a low-mode internal tide on the Tasman continental slope is investigated using simulations
10 of realistic and simplified topographies. The slope is super-critical to the internal tide, which should predict a
11 large fraction of energy reflected. However, the response to the slope is complicated by a number of factors:
12 the incoming beam is confined in space; it impacts the slope at an angle; there is a roughly cylindrical
13 rise directly offshore of the slope; and a leaky slope-mode wave is excited. These effects are isolated in
14 simulations that simplify the topography. In order to separate the incident from reflected signal, an incident
15 response without the reflector is subtracted from the total response to arrive at a reflected signal. The real
16 slope reflects approximately 65% of the mode-1 internal tide as mode-1, less than two-dimensional linear
17 calculations predict, due to the three-dimensional concavity of the topography. It is also less than recent
18 glider estimates, likely due to along-slope inhomogeneity. The inhomogeneity of the response comes from
19 the Tasman Rise which diffracts the incoming tidal beam into two beams, one focused downstream, and
20 one diffracted to the north. Along-slope inhomogeneity is enhanced by a partially trapped super-inertial
21 slope wave that propagates along the continental slope, locally removing energy from the internal tide and
22 re-radiating it further north. This wave is present even in a simplified straight-slope topography, and its
23 character can be predicted from linear resonance theory.

²⁴ 1. Introduction

²⁵ Energy is lost from the surface tide when it interacts with topography and, in the deep ocean, is largely
²⁶ redistributed as an internal tide. The fate of the internal tide is unclear, but depends on the dominant
²⁷ wavelengths that are forced. Gentle topography that is subcritical to the internal tide is likely dominated by
²⁸ higher vertical modes and is thought to break via wave-wave interactions relatively close to the topography
²⁹ (i.e. Polzin 2009; St. Laurent and Garrett 2002). Steeper supercritical topography, while exhibiting signif-
³⁰ icant local dissipation, tends to radiate a large fraction of the internal tide away from the topography as
³¹ low-mode waves (i.e. at Hawaii; Klymak et al. 2006; Carter et al. 2008). Given that a significant fraction of
³² the internal tide energy is generated at steep topography (Legg and Klymak 2008), and that the distribution
³³ of the mixing it eventually drives has impacts on understanding the distribution of ocean properties and the
³⁴ strength of the overturning circulation (i.e. Melet et al. 2013), it is desirable to understand where and how
³⁵ the radiated energy dissipates.

³⁶ One candidate sink for the low-mode internal tide is scattering and dissipation from continental slopes.
³⁷ These slopes are known to be hotspots of turbulent mixing from the few observational studies to date (Nash
³⁸ et al. 2007; Klymak et al. 2011; Martini et al. 2013). However, these studies have also demonstrated some
³⁹ of the difficulties in tracking internal tide energy on these slopes. Net internal-tide fluxes are relatively
⁴⁰ straight forward to measure, but ideally we would like to separate the incident and reflected fluxes if a
⁴¹ parameterization of turbulence on the slope is to be made, since the incident fluxes are what drive the
⁴² turbulence. The reflectivity of a continental slope is the ratio of the energy flux convergence divided by the
⁴³ total incident flux:

$$R = \frac{F_{out}}{F_{in}}, \quad (1)$$

⁴⁴ where F is depth-integrated for a two-dimensional budget or line-integrated for a three-dimensional one.
⁴⁵ Even simple two-dimensional linear models of reflection indicate that determining the reflectivity will be
⁴⁶ challenging, with reflection co-efficients strongly depending on the modal content and phases of the incident
⁴⁷ internal tides (Klymak et al. 2011) and the local surface tide (Kelly and Nash 2010). These linear models
⁴⁸ have been used globally to estimate reflection co-efficients for the mode-1 tides on realistic continental slope
⁴⁹ bathymetries, (Kelly et al. 2013b,a), but these calculations assume the incoming tide is known, and that the

50 topography is relatively homogenous over a distance similar to the mode-1 horizontal wavelength.

51 Determining the incident flux, F_{in} , from field data, and even from a numerical model with sufficient
52 complexity, is not trivial. In two dimensions, or with simple plane wave geometries, it is straight forward
53 to fit incident and reflected plane waves to recover the desired reflection co-efficient (figure 1a). In the real
54 ocean, even if tidal signals can be separated from confounding influences, internal tides are often spatially
55 inhomogeneous, and form lateral “beams” (in x-y; Rainville et al. 2010) that make plane wave fits difficult
56 from a finite array of moorings; for instance a mooring array could be located more in the incoming beam
57 than in the reflected, leading to an exaggeration of the computed energy convergence (figure 1b). Plane-wave
58 fits to satellite altimetry tracks are promising, but will also suffer from a lack of fidelity if the internal tides
59 are inhomogeneous on the scale of the plane wave fits (Zhao and Alford 2009). In the model, high resolution
60 temporal and spatial information makes it possible to separate signals spectrally according to their direction
61 of propagation (i.e. using a Hilbert transform, Mercier et al. 2008), but this method works best if there are
62 no boundaries and the signals at the edges of the model domain can be tapered to reduce Gibbs ringing,
63 neither of which are applicable in the nearfield of a continental slope.

64 The region considered here is the Tasman continental slope, the focus of a concentrated internal tide
65 field experiment. As preliminary work, it has been sampled continuously by gliders for a number of months
66 in 2012 and 2013 (Johnston et al. 2015). The gliders were flown to form and antenna over which internal
67 plane-wave fits were made. These efforts show a standing wave pattern, with amplitudes and phases as one
68 would expect for internal waves incident on the slope from the southeast where internal tides are expected to
69 be generated from the Macquarie Ridge (figure 2a). The amplitudes of the interfering waves were such that
70 the reflectivity is predicted to be high on this slope, with estimates of 0.7 to 1.0 from the arrays (Johnston
71 et al. 2015). The gliders also picked up a 100-km wavelength wave propagating along slope towards the
72 north, a finding we isolate and discuss below.

73 Here we run numerical simulations that are meant to represent a mode-1 internal M_2 tide incident on the
74 Tasman Slope, east of Tasmania. The simulations are only forced by the incident internal tide, and there is
75 no local forcing, allowing the reflection signal to be isolated. After discussing the model setup section 2, we
76 briefly consider the response this forcing has on the slope section 3 and compute and energy budget of the

77 complete response. In order to separate the physics of the reflection, we then simplify the geometry section 4,
78 both geometrically, and by removing parts of the topography. This technique allows us to separate incident
79 and reflected signals from the total response without appeal to plane wave fits. We end with a discussion of
80 the results (section 5) where we note the applicability of two-dimensional reflection models and discuss the
81 leaky slope waves evident in the simulations. We conclude with a summary (section 6).

82 2. Model setup

83 a. Basics

84 The numerical model used here is the MITGCM (Marshall et al. 1997), visualized using the Python
85 scientific stack (Hunter 2007; van der Walt et al. 2011). The setup is very similar to Buijsman et al. (2014),
86 with the model run in hydrostatic mode, background (isotropic) diffusivities and viscosities of $10^{-5} \text{ m}^2 \text{ s}^{-1}$,
87 and enhanced diffusivity and viscosity in regions of temporarily unstable stratification (Klymak and Legg
88 2010). A second-order flux-limiting temperature advection scheme is used which results in some numerical
89 dissipation and diffusion. Sensitivity tests were run with weaker forcing, and the fraction of energy dissipated
90 in the model did not change, indicating that the dissipation highlighted below is dominated by numerical
91 dissipation due to the lack of lateral resolution (1 km) rather than explicit viscosities. Dissipation is not the
92 main focus of this paper, and finer resolutions have been used for more focused efforts dealing with turbulence
93 on the slope (in preparation). These simulations are therefore the most “linear” that the resolution will allow.

94 Topography is from a data set that combines Smith and Sandwell (1997) and multibeam data from
95 Australian surveys (Whiteway 2009) (figure 2b). For this paper, we use a Cartesian co-ordinate system
96 centered at 44 S, 148 E, with y pointing 12 degrees east of geographic north (magenta lines, figure 2). This
97 co-ordinate system is close to cross-slope in the x-direction, and is used for conceptual convenience. The
98 simulations are run on a f-plane ($f = -10^{-4} \text{ s}^{-1}$).

99 A 1-km lateral resolution is used along the continental slope (figure 3a, smallest inset green box). Res-
100 olution is expanded by 3.5% per grid cell beyond the 1km-resolution region, to a maximum of 5 km in the
101 second largest inset box (figure 3a); this keeps the resolution over the Tasman Rise and the rest of the

102 continental slope at least 5 km. Further out, the grid spacing is again increased at 3.5% per grid cell until
 103 a maximum grid cell size of 10 km is reached.

104 Vertical resolution is approximately stretched so $dz \sim 1/N$, where $N^2(z) = -\frac{g}{\rho_0} \frac{d\rho}{dz}$ is the vertical strati-
 105 fication. 200 vertical grid cells are used for these simulations. The vertical stratification is from the World
 106 Ocean Atlas for the Tasman Sea just offshore of Tasmania (Boyer et al. 2013), and is assumed laterally
 107 constant in the domain. This precludes any mesoscale effects, which are believed to be important in this
 108 area, and are the subject of future work.

109 *b. Forcing*

110 To simplify the generation problem we apply an analytical forcing to our model. This is composed of
 111 two line sources at approximately the location of the Macquarie Ridge (figure 3a). The initial conditions
 112 and the southern and eastern boundaries of the model were set with this forcing. The forcing is similar to
 113 that suggested by Rainville et al. (2010), except instead of a single point source placed a distance R from
 114 the line source, the line source is digitized as a number of discrete point sources and their response in the
 115 domain summed. The mode-1 pressure anomaly is given by:

$$116 p'(x, y, t) = \sum_{i=1}^N a_i \exp(j(|k_t|r_i - \omega t)) \quad (2)$$

117 where $r_i = \sqrt{(x - x_i)^2 + (y - y_i)^2}$ is the distance to the source, and $|k_t|$ is the absolute value of the mode-1
 wavenumber:

$$118 k_t = \frac{(\omega^2 - f^2)^{1/2}}{c_e} \quad (3)$$

119 where ω is the frequency of the tide, f is the Coriolis frequency, and c_e is the eigenspeed of the vertical mode
 equation:

$$120 \frac{d}{dz} \left(\frac{1}{N^2} \frac{d\psi}{dz} \right) + \frac{1}{c_e^2} \psi(z) = 0. \quad (4)$$

121 Here $\psi(z)$ is the eigenfunction that sets the shape of the vertical mode, and the boundary conditions are
 $d\psi/dz = 0$ at $z = 0$ and $z = -H$, where H is the water depth. For convenience, we normalize $\psi_m(z)$ so that

$$122 \int_{-H}^0 \psi_m(z) \psi_n(z) dz = \delta_{mn}. \quad (5)$$

122 Horizontal velocities can be linearly decomposed by these shapes, as can the pressure signal.

123 To compute the wavefield, the horizontal velocity components are derived from the internal wave consistency relations:

$$u(x, y, t) = \sum_{i=1}^N \frac{k_x \omega + j k_y f}{\omega^2 - f^2} \frac{p'_i}{\rho} \quad (6)$$

$$v(x, y, t) = \sum_{i=1}^N \frac{k_y \omega - j k_x f}{\omega^2 - f^2} \frac{p'_i}{\rho} \quad (7)$$

125 where $k_x = k_t \cos(\theta_i)$ and $k_y = k_t \sin(\theta_i)$ are calculated from the angle to each element of the line sources
126 $\theta_i = \arctan((y - y_i)/(x - x_i))$.

127 The resulting incoming wavefield (figure 3a) has a beam of energy flux that radiates northwest, and is
128 relatively tightly focused. The interference pattern creates a null to the south and north, and a secondary
129 beam that radiates due west. This schematic agrees with more realistic regional tidal models (H. Simmons,
130 in preparation), and the amplitude of the beam was tuned to give approximately 2 kW m^{-1} incident at
131 Tasmania. Note this is less than estimates from altimetry and numerical simulations, and is purposely low
132 to keep the runs as “linear” as possible. The initial condition is applied uniformly through the domain,
133 regardless of bathymetry, so there are some start-up transients as the proper baroclinic flow develops.

134 The northern and western boundaries are sponges where the velocity is slowly dropped to zero and the
135 stratification relaxed to the initial stratification (figure 3a, green rectangles). Our main focus is the area
136 from $y=0$ to 400 km, so the boundaries are sufficiently far that small residual reflections do not affect the
137 response.

138 The ideal response off the Tasman topography would be as a plane-wave reflection from a wall at $x = 0$ km
139 (i.e. Johnston et al. 2015). Here we have a relatively confined beam, but we can make a start by considering
140 the reflection the beam from a wall at $x = 0$ km for $y > 0$ km (figure 3b,c) using the method of images with
141 identical line sources mirrored about the y-axis, and their phase shifted by 180 deg. The reflection pattern
142 that sets up is not entirely regular, but has some straight-forward features. The incoming beam impacts the
143 wall at approximately 30 deg. The horizontal wavelength of an M_2 internal tide is 178 km, so the standing
144 wave in the x-direction will have a wavelength $178/\cos(30) \approx 200$ km and in the y-direction will have a
145 wavelength of approximately 350 km. These spatial scales are readily apparent in the analytical forcing

146 despite the non-plane-wave character of the idealized forcing (figure 3c). Note that the standing energy flux
147 (figure 3b) has peaks and nulls in absolute value, with the peaks having large flux to the north. The peaks
148 are every half cross-slope wavelength (i.e. 100 km). The nulls have weak southward energy flux (though it
149 is difficult to discern from the subsampled arrows in the plot).

150 3. Realistic model simulation

151 The response of the forcing in the most real bathymetry motivates the more idealized experiments that
152 follow. From the initial forcing (figure 4a), a complex wavefield develops with clear scattering from the
153 Tasman Rise, the shelf, and numerous small inhomogeneities on the sea floor (figure 4b–d). Looking along
154 slope, the phase of the velocity signal can be seen changing approximately every 200 km, and it changes
155 approximately every 100 km offshelf similar to what we expect from an oblique standing wave (compare
156 figure 4h to figure 3b). However the pattern is complicated, not lining up in the north-south direction and
157 inhomogeneities in the energy that are not accounted for by a simple two-wave model.

158 A time-averaged energy balance is performed online in the model using the terms outlined in Kang and
159 Fringer (2012); Kang (2011). The energy balance vertically integrated can be schematized as:

$$dE_{bc}/dt = -\nabla_H \cdot \mathbf{F}_{bc} + \text{Conversion} - \text{Dissipation}. \quad (8)$$

160 where E_{bc} is the depth-integrated baroclinic energy density, \mathbf{F}_{bc} is the depth integrated energy flux, including
161 both the pressure work term and the non-linear advection of energy (which is small in our runs). All quantities
162 are averaged over an M_2 tidal period. “Conversion” is a complex term representing transfer from barotropic
163 motions to baroclinic (Kang 2011, eq. 5.102) and includes the barotropic heaving of the water column, the
164 density anomaly, and a non-linear horizontal advection term. These non-linear terms can be non-trivial in
165 real bathymetry (Buijsman et al. 2014). The conversion term is positive if the barotropic tide loses energy
166 and the baroclinic tide gains energy. “Dissipation” is computed here as the residual, and includes dissipation
167 due to explicit viscosity, numerical dissipation, and bottom drag.

168 Of note in the energy calculation is that the largest local term in the energy budget is an alternating
169 pattern of barotropic-baroclinic conversion at the shelf break balanced by baroclinic flux convergences and

170 divergences (figure 5). The importance of the barotropic-baroclinic term can also be seen by considering the
171 x-integral of the energy budget from $x = -50$ km to $+100$ km (figure 6). Recall that the simulations have
172 no barotropic forcing. This coupling is catalyzed by a start-up transient hitting the slope with the incoming
173 internal tide beam, and continues throughout the simulation, and is a leaky super-inertial slope wave (see
174 section 5).

175 The time series of the energy terms integrated along the slope demonstrates that the barotropic-to-
176 baroclinic term is relatively small when averaged, with a small loss of energy from the baroclinic tide to the
177 barotropic in the integral region (figure 6b). The model is largely in a steady state by tidal cycle 15, with
178 some residual oscillations in dE/dt and the flux convergence. The large-scale baroclinic energy changes do
179 not change the dissipation residual very much, which is relatively constant after 5 tidal cycles. To put the
180 50 MW of dissipation into context, the initial energy that comes in the east and south sides of this analysis
181 box in the initial conditions is 315 MW, so the model is dissipating about 17% of the incoming energy.
182 However, note that the dissipation is not the focus of these model runs nor of this paper. The forcing here
183 is approximately a factor 3 lower than the real forcing, so its likely the fraction of dissipation at this site is
184 higher if real forcing is used.

185 The majority of the energy budget is in the first vertical mode (figure 6c). Net fluxes in the region directly
186 offshore of the shelf break ($0 < x < 80$ km, and $0 < y < 400$ km) are composed of substantial mode-1
187 energy converging on the slope (95 MW net), and some reflected energy escaping in higher modes (28.3 MW,
188 mostly in modes 2–4). The 95 MW net flux is made up of the incoming and reflected mode-1 energy, and
189 separating those terms is the subject of the next section. There is some incoming higher-mode energy as well
190 due to scattering from the Tasman Rise, but as we will also show below, this is minor. The spatial pattern
191 (not shown) of the mode conversion at the continental slope indicates hot-spots for conversion. Modes 2 and
192 4 have a hotspot of conversion near $y = 250$ km, and mode 3 at $y = 325$ km.

193 4. Simplified geometries

194 To help tease apart the effects of the Tasman Rise and the non-uniform slope, we carry out a few
 195 simplified experiments (figure 7; figure 8). The REAL case is the one discussed above (figure 8f). The NO
 196 TOPO case has no topography at all (figure 8a), just the beam being forced at the south and east boundaries
 197 and (mostly) absorbed at the west and north. RISE was run with the real bathymetry west of $x = 70$ km
 198 (figure 8e). Three idealized geometries simplify the physics even more: the SHELF case has a supercritical
 199 two-dimensional continental slope running north from $y = 0$ km (figure 8d). ROUND RISE is a 1700-m tall
 200 cylinder-shaped bump with radius of 50 km centered at approximately the same location as the Tasman Rise,
 201 with no shelf to the west (figure 8b). The simplified slope and the rise are both used in the SHELF/RISE
 202 case (figure 8c).

203 a. Shelf-only configuration

204 The simplest topography is the SHELF configuration (figure 8d). Here we have a response that is quite
 205 similar to the analytical response calculated above (figure 3b). The only difference between these two cases
 206 is the narrow shelf west of $x = 0$ km and the slight slope to the continental slope. The interference pattern
 207 between the incoming wave and the reflected wave is clear in this plot, with the same characteristic length
 208 scales as above, and a slight bending of the response due to the radial spreading of the beam.

209 The goal of this paper is to determine the amount of reflectivity of the continental slope. This is a hard
 210 number to determine in a complicated geometry, and naturally depends on the region of integration. For
 211 the SHELF configuration the situation is relatively simple, and we use it to illustrate the numerical technique
 212 used below. The signal in the full simulation is assumed to consist of an “incoming” signal and a reflected
 213 signal, so we can decompose the east-west velocity amplitude of the first vertical mode (for example) as:

$$u_1^t(x, y) = u_1^i + u_1^r \quad (9)$$

$$v_1^t(x, y) = v_1^i + v_1^r \quad (10)$$

$$p_1^t(x, y) = p_1^i + p_1^r \quad (11)$$

214 where u_1^t is the complex amplitude of the M_2 , mode-1 east-west velocity of the simulation with the reflection,

²¹⁵ u_1^i of the incoming signal, and u_1^r of the reflected signal. We assume for this example that the incoming
²¹⁶ signal u_1^i is given by the No TOPO simulation, and u_1^t is from the SHELF simulation. The reflected signal u_1^r
²¹⁷ is simply the difference of these two. This method has been used by Hall et al. (2013) for a two dimensional
²¹⁸ flow. Here it is an absolute necessity because of the complicated three-dimensional topography.

²¹⁹ In order to compute and energy budget, we consider that the energy fluxes are calculated from the
²²⁰ decomposed signals as:

$$F_{u1}^t = u_1^t p_1^t \quad (12)$$

$$= \overbrace{u_1^i p_1^i}^{Incoming} + \overbrace{u_1^r p_1^r}^{Reflected} + \overbrace{u_1^i p_1^r + u_1^r p_1^i}^{Cross Terms} \quad (13)$$

$$F_{v1}^t = v_1^t p_1^t \quad (14)$$

$$= \overbrace{v_1^i p_1^i}^{Incoming} + \overbrace{v_1^r p_1^r}^{Reflected} + \overbrace{v_1^i p_1^r + v_1^r p_1^i}^{Cross Terms} \quad (15)$$

²²¹ The cross terms are not negligible for any realistic forcing, and indeed give rise to the interference patterns
²²² seen above (Nash et al. 2004; Martini et al. 2007).

²²³ The “total” response (figure 9d) consists of the incoming response (figure 9a), and the “reflected” signal
²²⁴ (figure 9b), and substantial cross-terms (figure 9c). The cross terms are mostly perpendicular to the direction
²²⁵ of reflection (i.e. parallel to the slope) and alternately flux energy to the north and south every half cross-
²²⁶ slope wavelength. Combined, these three components give the “total” flux with net fluxes to the north in
²²⁷ alternating peaks every full offslope wavelength.

²²⁸ The reflected response (figure 9b) shows approximately what we would expect with energy being radiated
²²⁹ to the north-east. There is some concentration of this energy at $y \approx 75\text{km}$, and $y \approx 225\text{km}$ because of
²³⁰ coupling with a partially trapped slope wave. This coupling causes a redistribution of the reflected energy,
²³¹ focusing it approximately every along-slope wavelength of the slope wave (we show in section 5 that this
²³² wavelength changes as the slope geometry changes).

²³³ Performing this analysis for the lowest 10 modes, we arrive at an energy budget for the slope in the green
²³⁴ box in the figures ($0 < y < 400\text{ km}$, and $x < 80\text{ km}$; figure 9, inset budgets). Note that we assume the
²³⁵ flux through $x = 0$ is zero. With this calculation, we see that 408 MW is incident on the slope in mode-1.
²³⁶ There is also a net flux of 50 MW into this region from the cross terms. This is a redistribution of energy

237 from north of our box into the box. There is a net convergence of this cross-term energy because there is
238 dissipation in the box; in a purely inviscid solution this term should balance to zero over a closed box. If we
239 extend the integration further north, the cross-term flux drops to zero.

240 Most of the incoming energy reflects back out of the box (figure 9b), with the bulk remaining in mode
241 1, and some scattering to higher modes. This scattered energy radiates to the north east (not shown). The
242 mode-1 reflection is affected by the slope wave that transfers energy to and from the barotropic tide along
243 the slope, resulting in nulls and peaks in the mode-1 reflection.

244 *b. Tasman Rise only*

245 The Tasman Rise has a profound effect on the energy that impacts the continental slope (figure 8e and
246 f). The incoming beam is almost 500 km wide at $x = 0$ if there is no Tasman Rise, but breaks into three
247 narrower beams when there is a Tasman Rise (figure 8e). Upstream of the rise, the effect is somewhat less
248 energy propagating westward, with an interference pattern towards the east indicating some back reflection.

249 This pattern can be explained in terms of diffraction of the internal tide beam from a deep obstacle (i.e.
250 Johnston and Merrifield 2003). There is a down-wave concentration of energy along the seamount's axis,
251 a null, and sidelobes to the north and south. In this case, the incident beam is of comparable size to the
252 obstacle, leading to an asymmetry, and a stronger lobe to the north than south.

253 Most of the response due to the Tasman Rise can be modeled simply as a cylindrical obstacle in the
254 beam (figure 8b and c). Here our obstacle is 1800 m high in 5000 m of water, and has a radius of 50 km
255 (figure 7). This captures most of the features of the actual Tasman Rise, despite not having a shallow spire
256 in the center and being slightly smaller than the real Rise. The differences make the simplified response
257 have weaker nulls and the whole response is directed a bit further north than the real Rise. Adding the shelf
258 (figure 8c) yields a response that bears substantial similarity to the REAL forcing case.

259 Decomposing into an incoming and reflected signal (figure 10) demonstrates the effect of the Tasman
260 Rise on the response. Less energy is incident on the control volume, largely because the diffraction redirects
261 some of that energy to the north of $y = 400$ km. There is a strong reflection of energy where the main
262 diffraction lobe reflects from the slope (figure 10b), and a smaller maximum just to the north ($y = 250$ km)

263 due to the along-slope wave that is strummed. There is a reflection further north where the northern lobe
264 of the diffraction pattern reflects.

265 The incoming energy has some more high-mode content due to scattering at the cylindrical rise (fig-
266 ure 10a), though it is still 95% mode-1. The reflection is almost 80% mode-1, with some scattering to higher
267 modes. The net flux shows approximately 15% of the incoming energy is dissipated at the shelf.

268 *c. Real Case*

269 The REAL forcing is similar, if more complex (figure 11). The simulation using the bathymetry in the
270 RISE ONLY case (figure 8e) is used as the “Incoming” energy flux, and the REAL (figure 8f) case is the
271 “Total”. Compared to the cylindrical rise, the real Tasman Rise creates a sharper diffraction pattern, and
272 more back reflection. However, the REAL simulation has many of the same features as the SHELF/RISE
273 simulation (figure 8c).

274 Slightly less incoming energy passes into the control volume (figure 11a) because the diffraction by the
275 real Tasman Rise is sharper than the cylindrical rise. As for the cylindrical rise case, there is some incoming
276 higher mode energy due to forward scattering, though again over 95% is mode-1. Reflection is concentrated
277 near $y = 125$ km and $y = 450$ km, associated with the diffraction nodes, with about 85% in mode 1
278 (figure 11b). Dissipation is less than 25% of the incoming energy (figure 11d).

279 **5. Discussion**

280 *a. Estimating reflection co-efficients*

281 A major goal of this effort is estimating the fraction of incoming tide that is reflected by the Tasman
282 continental slope to come up with a reflectivity co-efficient. Here we discriminate between the mode-1
283 reflection, $R_1 = F_{ref,1}/F_{in,1}$, and the total reflection into all the modes, $R_T = F_{ref}/F_{in}$. Evaluating these
284 co-efficients is less straightforward than it may sound because it is difficult to separate the incoming from
285 reflected signal in complicated geometry, even in a fully resolved numerical model, let alone in observations.

286 Above, we used an integrated measure, comparing the incoming flux from a model with no continental slope
287 to one with a continental slope and integrating the fluxes over a control volume from $y = 0$ to 400 km. This
288 control volume was an arbitrary choice, but yielded reflectivities of mode -1 internal tide $R_1 = 0.65$ and the
289 total internal tide of $R_T = 0.76$ (figure 11).

290 Determining reflectivity from a mooring array is significantly complicated by three-dimensionality and
291 along slope variability. From the mooring array in figure 11, the reflectivity is $R_1 = 0.6/1.3 = 0.46$, a
292 significant under-estimate. The reason for this should be relatively clear from looking at figure 11a,b; the
293 mooring array nicely captures the northward diffracted ray, but catches some of the reflected pattern from
294 the main beam to the south. There are significant interferences in the reflected patterns (figure 11b) because
295 the reflected pattern is a complicated superposition of the cylindrically spreading reflections along the slope.

296 Determining the reflectivity as a function of along-slope direction y is difficult. Simply lining up the
297 onslope fluxes does not yield useful results because the reflection from any given point on the slope radiates
298 cylindrically, and it is necessary to integrate over volumes. Here we take the same approach as used in the
299 previous section (i.e. figure 11), but integrate over smaller control volumes (80 km in y) to see the reflectivity
300 as a function of y (figure 12a,b). The incoming flux every 80 km shows the diffracted beam pattern with
301 a maximum net incoming flux at $y = 120$ km (figure 12a, red line) and a secondary peak to the north at
302 about 440 km. The net reflectivity from these boxes ranges from 0.8 to a low of almost zero at $y = 280$ km
303 (figure 12b, solid blue line). Note an uncertainty in the flux decomposition associated with the flux in the
304 cross terms (figure 12a, purple line). This term does not balance to zero, and forms a significant part of the
305 energy budget over such small control volumes. It cannot be uniquely decomposed into either the incoming
306 or reflected energy terms, so remains as an uncertainty.

307 In two-dimensions, the fraction of the tide reflected into mode 1 (and higher) can be predicted from linear
308 theory using the method described by Kelly et al. (2013a) of matching Laplacian tidal solutions at discrete
309 steps on a discretized topography. If the tide is obliquely incident on the slope, there can be substantial
310 differences in the reflected tide (Kelly et al. 2013b). If we run these solutions for the Tasman Slope with an
311 incident angle of 30 degrees, the reflectivity into mode-1, R_1 is similar to the numerical simulation (figure 12b,
312 thick black line). The predicted reflectivity is greater for most of the ridge, but the null at $y = 250$ km is

313 captured.

314 The REAL simulation has a mode-1 reflectivity of $R_1 = 0.65$. A naive average of the reflectivity from the
315 linear model between $y = 0$ and 400 km yields $\langle R_1 \rangle = 0.71$. However, that does not take into account the
316 varying strength of the incoming diffracted beam, which is stronger where the reflectivity is higher. Weighting
317 by the incoming beam strength, then the reflectivity averages $\langle R_1 \rangle_{beam} = 0.8$, and is substantially larger
318 than in the numerical simulations.

319 An attempt has been made to estimate reflectivity from this site from autonomous gliders surveys (John-
320 ston et al. 2015). First, the gliders saw a substantial concentration of energy shoreward of the Tasman
321 Rise. This is a feature of the model, and clearly explained by the diffraction of energy by the Tasman Rise
322 (figure 11).

323 For the region in the lee of the Tasman Rise, Johnston et al. (2015) estimate a reflectivity of the mode-1
324 internal tide of between 0.8 to 1.0 by fitting plane waves to the velocity and displacement amplitudes and
325 phases. If we confine our incoming versus outgoing energy budget to the region $80 \text{ km} < y < 200 \text{ km}$,
326 representative of their *Spray 56* deployment, we calculate a reflectivity of 0.7, which is lower than their
327 lowest estimate of 0.8, and much lower than their high estimate of 1.0. A second deployment, *Spray 55*,
328 covered more of the slope (up to $y = 300 \text{ km}$). In this domain, they estimate a reflectivity of 0.6. This is in
329 agreement with the numerical simulation, which achieves the same result from $0 \text{ km} < y < 300 \text{ km}$.

330 The directions of wave propagation fit from the glider data is not in agreement with the model. The fits
331 to the *Spray 55* data show incoming energy at between 125 and 145 degrees, which is similar to the model.
332 However the reflection is slightly south of due east (0 to -30 degrees geographic), whereas the numerical model
333 is definitely to the northeast far from shore. An explanation is evident from close inspection of figure 11b
334 between the Tasman Rise and the continental slope where the glider spent the most time. At this location
335 the off-shore energy flux is almost exactly in the x-direction, (-12 degrees geographic), in agreement with
336 the glider observations.

337 Finally, one of the gliders (*Spray 56*) picked out a northward propagating disturbance along the conti-
338 nental slope with wavelength of 100 km. This wavelength matches the wavelength of the slope wave seen in
339 the real simulations (figure 5a,b). Interestingly, they only pick this wavelength out in vertical displacement

340 data, not in velocity.

341 *b. Slope wave importance and dynamics*

342 The structure of the barotropic-to-baroclinic conversion on the slope is an intriguing feature of these
343 simulations, and appears in regional simulations (Simmons, in prep) and the glider data (Johnston et al.
344 2015). Here, it shows up most clearly in the SHELF simulations because of the simplified bathymetry.
345 However, it is also clear in the REAL simulation (figure 5a). This slope wave redistributes energy in the
346 reflected baroclinic response (figure 9), taking a relatively homogenous incoming energy source and focusing
347 the reflection every 200 km or so along slope.

348 This wave is a slope mode that is strummed by the incident internal tide at the “corner” of the topography
349 ($x = 0$, $y = 0$); a long slope without the corner does not excite this wave, nor does an internal tide
350 coming directly from the east and hitting the topography at a normal angle. The along-slope wavelength is
351 independent of the incident along-slope wavelength in the open water (tested by changing the angle of the
352 incident tide; not shown), and is a robust feature of the slope shape. A sensitivity experiment that varied
353 the continental slope widths demonstrates that narrower slopes strum longer along-slope waves (figure 13).

354 These waves are super-inertial and are an example of partially trapped slope waves (Dale and Sherwin
355 1996; Dale et al. 2001). We compare the wavelength of the slope waves (figure 14, thick lines) to the
356 empirical modes predicted from linear theory (Dale et al. 2001). The procedure solves for the response of
357 the flow in the coastal bathymetry due to forcing with varying along-slope wavelengths. Resonant along-
358 slope wavelengths lead to a much stronger response (Appendix and figure 14, thin lines). The along-slope
359 wavelength of the resonant modes in the linear calculation agree quite well with the wavelengths of the
360 fully non-linear solutions. Narrower continental slopes yield longer along-slope wavelengths, and the spatial
361 modes that correspond to the peaks are similar to deep-ocean mode-1 off the slope.

362 The slope wave is an important term in the local energy budget when compared the incoming and
363 reflected energy fluxes (figure 15). The incoming energy peaks at 1.2 kW/m, and the reflected energy is of a
364 similar magnitude but with oscillations at twice the wavelength of the slope wave. The integrated barotropic-
365 baroclinic conversion is as high as 0.4 kW/m-coastline, and leads to 0.4 kW/m peak-to-peak oscillation in

366 the reflected energy (its not 0.8 kW/m peak-to-peak because the reflected energy spreads spherically by 40
367 km, where the reflected flux is evaluated, figure 9). This turns even a relatively straight slope into a series of
368 internal tide absorbers and radiators, leading to 100-km scale inhomogeneity in the reflected internal tide.

369 6. Summary

370 A mode-1 internal tide was launched at a variety of topographies representing the Tasmanian continental
371 slope. The goal was to determine the “reflectivity” of this slope, in terms of the modal content of the
372 reflected energy and the local dissipation. The latter is somewhat suspect in this model because of crude
373 lateral resolution, but the REAL simulation indicated that 21% of the incoming energy was dissipated, and
374 65% was reflected as mode-1 energy. The incoming internal tide flux used here was weak compared to the
375 flux modeled and inferred from altimetry in the Tasman Sea, so we expect the dissipation in more realistically
376 forced models to increase.

377 Despite a simple incoming internal tide that is linear, semi-diurnal, and mode-1, we have found a rich
378 and complex response of the topography when the remote wave impacts the topography. The response can
379 be characterized as follows:

- 380 • diffraction of the beam by the Tasman Rise,
381 • oblique reflection from the continental slope,
382 • and a leaky slope wave response that redistributes reflected internal energy along-slope.

383 Of these, perhaps only the second effect was expected before carrying out the simulations. However, as we
384 saw above, even the reflection problem is significantly complicated in the presence of three-dimensionality.

385 Diffraction around underwater topography should have been expected, however, the relative depth of the
386 obstacle makes it surprising that the effect is so strong. The fact that the lateral width of the Tasman Rise
387 is close to the wavelength of the incoming internal tide makes predicting the diffraction pattern difficult.
388 Baines (2007) considers generation of internal tides at seamounts, but does not deal with scattering and
389 diffraction. The problem is similar to electromagnetic waves passing through a wire, but a linear response

390 for that problem is not trivial to compute (i.e. Bonod et al. 2005), and still does not have a confined vertical
391 mode structure as we find in the internal wave problem.

392 The excitation of slope waves has been explored by Dale et al. (2001). It has an important effect on the
393 redistribution of energy along slope. The redistribution affects where high dissipation is found in the model
394 (figure 5), and adds more inhomogeneity to the reflected internal tide.

395 The complexity grows if other real-world influences are to be accounted for. The East Australian Current
396 flows along this slope, varying the stratification in the horizontal, provides lateral shears that can distort the
397 internal tide response, and carrying eddies that can add a strong time dependence to these effects. Even in
398 two dimensions, the strength of the internal tide reflection can be significantly impacted by the phase of the
399 incoming tide with other baroclinic modes Klymak et al. (2011) or the barotropic (Kelly and Nash 2010). The
400 simulations here exclude the local barotropic tide, so this would certainly complicate the reflected response.
401 Finally, the internal tide used here was monotonic, whereas the real tide will also have other frequencies,
402 most notably subinertial diurnal frequencies that will have trapped wave responses (personal communication,
403 R. Musgrave).

404 Regardless, it is useful to have studied the “simplest” response we could in this system to tease apart
405 the dominant physics. This response is complex, and it should be clear that solely observational efforts to
406 balance a reflection budget are going to be a challenge. Merging simulations and observations is a likely way
407 forward in understanding the wave field in this complex slope region.

408 With respect to the reflection problem, the modeled slope has a relatively high reflection back into the
409 open ocean, with as much as 65% of the incoming energy being reflected as mode-1. Its possible that higher
410 resolution runs will be more dissipative, and that stronger forcing will lead to a higher fraction of dissipation.
411 However, these simulations, and the results from the rest of the experiment to date (i.e. Johnston et al. 2015)
412 indicate that bulk of the energy from the Macquarie Ridge must dissipate elsewhere.

413 *Acknowledgments.*

414 Our thanks to conversations with Andy Dale on leaky slope waves and Qiang Li for sharing his linear
415 code for the Lindzen-Kuo method. J. Klymak was supported by the Canadian National Science Engineering

⁴¹⁶ Research Council Discovery Grant 327920-2006, and by computer time from the US Office of Naval Research,
⁴¹⁷ T. Palusziewicz, program officer. H. Simmons and D. Brazhnikov were supported by NSF award 1130048
⁴¹⁸ to the University of Alaska Fairbanks. A website for this paper with analysis scripts, intermediate data files,
⁴¹⁹ and model setups is at <http://web.uvic.ca/~jklymak/ttide15>.

APPENDIX

422 Appendix Slope-wave calculation

423 The slope wave calculation follows the calculation made by Dale et al. (2001), where there are more details.

424 The linear equation for the pressure perturbations are assumed to have form $P = p(x, z) \exp^{i(k_y y - \omega t)}$, where

425 k_y is the along-slope wavenumber.

$$(f^2 - \omega^2) \frac{\partial}{\partial z} \left(\frac{\partial p / \partial z}{N^2 - \omega^2} \right) + \frac{\partial^2 p}{\partial x^2} - k_y^2 p = 0 \quad (\text{A1})$$

426 Subject to boundary conditions at the surface of $\partial p / \partial z = 0$ and at the sea floor of

$$\left(\frac{\omega^2 - f^2}{N^2 - \omega^2} \right) \frac{\partial p}{\partial z} = \frac{\partial h}{\partial x} \left(\frac{\partial p}{\partial x} - \frac{fk_y}{\omega} p \right) \quad (\text{A2})$$

427 The coast is assumed to be a wall, and the open ocean to consist of waves radiating away from the slope, or

428 if k_x , the cross-slope wavenumber, is imaginary, disturbances that decay away from the slope.

429 The above are discretized on a domain that is 260 km wide into 261 grid cells in x , and onto a sigma-

430 co-ordinate with 192 vertical levels. The hyperbolic method of solution due to Lindzen and Kuo (1969) was

431 used to solve on this domain for p for $\omega = 1.4f$, $f = 10^{-4}\text{s}^{-1}$, and for a sweep of k_y . Under an arbitrary

432 forcing certain values of k_y resonate and lead to stronger amplitude responses in p corresponding to spatial

433 modes of the system. The numerical method is sensitive to the stratification, so we used a fit exponential of

434 $N^2(z) = 2 \times 10^{-5}\text{s}^{-2} e^{z/(1000 \text{ m})}$ (where z is negative downwards). The scan was taken over 300 wavelengths

435 equally spaced between 30 and 180 km.

436 The resulting spatial modes are similar to those in Dale et al. (2001) (figure 16). There is a peak of

437 amplitude on the shelf, and then a second peak on the slope. As the slope gets more narrow, the peak on

438 the slope becomes broader. These shapes are the lowest modes.

439 The general code to solve this is at <https://github.com/jklymak/LindzenKuo>. The exact code used

440 for this paper is with the rest of the supplemental material.

REFERENCES

- 443 Baines, P. G., 2007: Internal tide generation by seamounts. *Deep Sea Res. I*, **54** (9), 1486 – 1508, doi:
 444 10.1016/j.dsr.2007.05.009.
- 445 Bonod, N., E. Popov, and M. Nevière, 2005: Differential theory of diffraction by finite cylindrical objects.
 446 *JOSA A*, **22** (3), 481–490, doi:10.1364/JOSAA.22.000481.
- 447 Boyer, T., et al., 2013: *World Ocean Database 2013*. NOAA Atlas NESDIS 72, doi:10.7289/V5NZ85MT.
- 448 Buijsman, M. C., et al., 2014: Three-dimensional double-ridge internal tide resonance in Luzon Strait. *J.*
 449 *Phys. Oceanogr.*, **44** (3), 850–869, doi:10.1175/JPO-D-13-024.1.
- 450 Carter, G., et al., 2008: Energetics of M 2 Barotropic-to-Baroclinic Tidal Conversion at the Hawaiian Islands.
 451 *Journal of Physical Oceanography*, **38** (10), 2205–2223, doi:10.1175/2008JPO3860.1.
- 452 Dale, A. C., J. M. Huthnance, and T. J. Sherwin, 2001: Coastal-trapped waves and tides at near-inertial
 453 frequencies. *J. Phys. Oceanogr.*, **31** (10), 2958–2970, doi:10.1175/1520-0485(2001)031<2958:CTWATA>2.
 454 0.CO;2.
- 455 Dale, A. C. and T. J. Sherwin, 1996: The extension of baroclinic coastal-trapped wave theory to superinertial
 456 frequencies. *J. Phys. Oceanogr.*, **26** (11), 2305–2315, doi:10.1175/1520-0485(1996)026<2305:TEOBCT>2.
 457 0.CO;2.
- 458 Hall, R. A., J. M. Huthnance, and R. G. Williams, 2013: Internal wave reflection on shelf slopes with
 459 depth-varying stratification. *J. Phys. Oceanogr.*, **43** (2), 248–258, doi:10.1175/JPO-D-11-0192.1.
- 460 Hunter, J. D., 2007: Matplotlib: A 2D graphics environment. *Comput. Sci. Eng.*, **9** (3), 90–95, doi:10.1109/
 461 MCSE.2007.55.
- 462 Johnston, T. M. S., D. L. Rudnick, and S. M. Kelly, 2015: Standing internal tides in the Tasman Sea
 463 observed by gliders. *J. Phys. Oceanogr.*, **45** (11), doi:10.1175/JPO-D-15-0038.1.

- 464 Johnston, T. S. and M. A. Merrifield, 2003: Internal tide scattering at seamounts, ridges, and islands. *J.*
 465 *Geophys. Res.*, **108** (C6), 3180, doi:10.1029/2002JC01528.
- 466 Kang, D., 2011: Barotropic and baroclinic tidal energy. Ph.D. thesis, Stanford University.
- 467 Kang, D. and O. Fringer, 2012: Energetics of barotropic and baroclinic tides in the Monterey Bay area. *J.*
 468 *Phys. Oceanogr.*, **42** (2), 272–290, doi:10.1175/JPO-D-11-039.1.
- 469 Kelly, S. and J. Nash, 2010: Internal-tide generation and destruction by shoaling internal tides. *Geophys.*
 470 *Res. Lett.*, **37**, L23611, doi:10.1029/2010GL045598.
- 471 Kelly, S. M., N. L. Jones, and J. D. Nash, 2013a: A coupled model for Laplace's tidal equations in a fluid
 472 with one horizontal dimension and variable depth. *J. Phys. Oceanogr.*, doi:10.1175/JPO-D-12-0147.1.
- 473 Kelly, S. M., N. L. Jones, J. D. Nash, and A. F. Waterhouse, 2013b: The geography of semidiurnal mode-1
 474 internal-tide energy loss. *Geophys. Res. Lett.*, doi:10.1002/grl.50872.
- 475 Klymak, J., M. Alford, R. Pinkel, R. Lien, Y. Yang, and T. Tang, 2011: The breaking and scattering of the
 476 internal tide on a continental slope. *J. Phys. Oceanogr.*, **41**, 926–945, doi:10.1175/2010JPO4500.1.
- 477 Klymak, J. M. and S. M. Legg, 2010: A simple mixing scheme for models that resolve breaking internal
 478 waves. *Ocean Modell.*, **33** (3-4), 224 – 234, doi:10.1016/j.ocemod.2010.02.005.
- 479 Klymak, J. M., et al., 2006: An estimate of tidal energy lost to turbulence at the Hawaiian Ridge. *J. Phys.*
 480 *Oceanogr.*, **36**, 1148–1164, doi:10.1175/JPO2885.1.
- 481 Legg, S. and J. M. Klymak, 2008: Internal hydraulic jumps and overturning generated by tidal flow over a
 482 tall steep ridge. *J. Phys. Oceanogr.*, **38** (9), 1949–1964, doi:10.1175/2008JPO3777.1.
- 483 Lindzen, R. and H.-L. Kuo, 1969: A reliable method for the numerical integration of a large class of ordi-
 484 nary and partial differential equations. *Mon. Wea. Rev.*, **97** (10), 732–734, doi:10.1175/1520-0493(1969)
 485 097⟨0732:ARMFTN⟩2.3.CO;2.

- 486 Marshall, J., A. Adcroft, C. Hill, L. Perelman, and C. Heisey, 1997: A finite-volume, incompressible Navier-
487 Stokes model for studies of the ocean on parallel computers. *J. Geophys. Res.*, **102** (C3), 5753–5766,
488 doi:10.1029/96JC02775.
- 489 Martini, K., M. Alford, J. Nash, E. Kunze, and M. Merrifield, 2007: Diagnosing a partly standing internal
490 wave in Mamala Bay, Oahu. *Geophys. Res. Lett.*, **34** (17), L17604, doi:10.1029/2007GL029749.
- 491 Martini, K. I., M. H. Alford, E. Kunze, S. M. Kelly, and J. D. Nash, 2013: Internal bores and breaking internal
492 tides on the Oregon continental slope. *J. Phys. Oceanogr.*, **43**, 120–139, doi:10.1175/JPO-D-12-030.1.
- 493 Melet, A., R. Hallberg, S. Legg, and K. Polzin, 2013: Sensitivity of the ocean state to the vertical distribution
494 of internal-tide-driven mixing. *J. Phys. Oceanogr.*, **43** (3), 602–615, doi:10.1175/JPO-D-12-055.1.
- 495 Mercier, M. J., N. B. Garnier, and T. Dauxois, 2008: Reflection and diffraction of internal waves analyzed
496 with the Hilbert transform. *Phys. Fluids*, **20** (8), 086601, doi:10.1063/1.2963136.
- 497 Nash, J., M. Alford, E. Kunze, K. Martini, and S. Kelley, 2007: Hotspots of deep ocean mixing on the
498 Oregon continental slope. *Geophys. Res. Lett.*, **34**, L01605, doi:10.1029/2006GL028170.
- 499 Nash, J. D., E. Kunze, J. M. Toole, and R. W. Schmitt, 2004: Internal tide reflection and turbulent
500 mixing on the Continental Slope. *J. Phys. Oceanogr.*, 1117–1134, doi:10.1175/1520-0485(2004)034<1117:
501 ITRATM>2.0.CO;2.
- 502 Polzin, K. L., 2009: An abyssal recipe. *Ocean Modelling*, **30** (4), 298–309, doi:10.1016/j.ocemod.2009.07.007.
- 503 Rainville, L., T. Johnston, G. S. Carter, M. A. Merrifield, R. Pinkel, P. F. Worcester, and B. D. Dushaw,
504 2010: Interference pattern and propagation of the M_2 internal tide south of the Hawaiian Ridge. *J. Phys.*
505 *Oceanogr.*, **40** (2), doi:10.1175/2009JPO4256.1.
- 506 Smith, W. and D. Sandwell, 1997: Global sea floor topography from satellite altimetry and ship depth
507 soundings. *Science*, **277** (5334), 1956, doi:10.1126/science.277.5334.1956.
- 508 St. Laurent, L. and C. Garrett, 2002: The role of internal tides in mixing the deep ocean. *J. Phys. Oceanogr.*,
509 **32**, 2882–2899, doi:10.1175/1520-0485(2002)032<2882:TROITI>2.0.CO;2.

- 510 van der Walt, S., S. C. Colbert, and G. Varoquaux, 2011: The NumPy array: A structure for efficient
511 numerical computation. *Comput. Sci. Eng.*, **13** (2), 22–30, doi:10.1109/mcse.2011.37.
- 512 Whiteway, T., 2009: Australian bathymetry and topography grid, june 2009. scale 1:5000000. Tech. rep.,
513 Geoscience Australia, Canberra. doi:10.4225/25/53D99B6581B9A.
- 514 Zhao, Z. and M. H. Alford, 2009: New altimetric estimates of mode-1 M2 internal tides in the central North
515 Pacific Ocean. *J. Phys. Oceanogr.*, **39** (7), 1669–1684, doi:10.1175/2009JPO3922.1.

516 List of Figures

- 517 1 Schematic of the difficulty of quantifying reflecting fluxes in an inhomogeneous environment. 27
- 518 Plane waves are trivial. Inhomogeneous incoming waves or reflections are significantly more
- 519 difficult.
- 520 2 Location of TTide experiment: a) Energy flux in a regional numerical simulation. Color is
- 521 the absolute value of the flux, arrows its direction. The magenta box indicates the numerical
- 522 modeling domain used in this paper. b) Detail of the bathymetry on the Tasman slope. The
- 523 magenta lines indicate 100 km in the x-direction, and 300 km in the y direction in the modeling
- 524 domain used in this paper. 28
- 525 3 a) Forcing used to drive the models used in this paper. Two mode-1 internal wave sources
- 526 are located to the south east (blue lines). The model domain is rotated 12 degrees from
- 527 geographic so the shelf break approximately lies along $x = 0$. Typical model domain and
- 528 sponge region is indicated as green rectangles. The 250, and 3000-m isobaths are contoured.
- 529 Arrows show the direction of the energy flux, and are scaled by its strength. b) Energy flux
- 530 of analytical response of energy reflecting from a wall at $x = 0$, north of $y = 0$. c) Phase of
- 531 reflected response. 29
- 532 4 a)-d) Surface x-direction velocity for four snapshots. a) is the initial conditions (slightly
- 533 modified after a tidal cycle) and d) is the steady state. Grey contours are depths at 3000,
- 534 2000, 1000, and 250-m. e)-h) is depth-integrated baroclinic energy flux at the same time
- 535 periods, with arrows indicating direction. 30
- 536 5 Energy budget over the 19th tidal cycle of a) Barotropic to baroclinic conversion; b) Baro-
- 537 clinic energy flux convergence ($-\nabla F_{bc}$); c) rate of change of baroclinic energy; d) residual
- 538 representing the dissipation in the model $D = -\nabla \mathbf{F}_{bc} + \text{Conv.} - dE/dt$. The green box is the
- 539 region for the energy time series (figure 6b). 31

540 6 a) Integral in x to 80 km offshore of the energy terms in figure 5 for the REAL case. Note
541 that the barotropic-baroclinic term (red) is of the same order as the baroclinic convergence
542 (cyan) and the residual dissipation (gray) for most of the slope. b) Energy budget time series
543 for the “Real” case, tidally averaged, where time is normalized by $T = 12.4h$, between $y = 0$
544 to $y = 400$ km. There is still a small residual increase in the energy with time (purple),
545 representing the accumulation of high-mode energy in the region. Net barotropic-baroclinic
546 conversion (red) is small and negative, indicating a small net loss to the barotropic tide in
547 this region. The bulk of the budget is the balance between baroclinic flux convergence (blue)
548 and the residual “dissipation” (gray). c) Net flux in the box defined by $0 < x < 80$ km, and
549 $0 < y < 400$ km. Green is the value for the net flux (no modal decomposition). Blue bars are
550 the modal decomposition. There is a net incoming flux in mode 1 and net reflecting fluxes in
551 higher modes (primarily modes 2-4).

32

552 7 Cross sections of topographies from $y = 50$ km.

33

553 8 Energy flux for six geometries at tidal cycle 20. Grey depth contours are -3000, -2000, -1000
554 and -250 m. Arrows indicate the direction of energy flux. See figure 7 for bathymetry cross
555 sections at $y = 50$ km.

34

556 9 Mode-1 decomposition of energy fluxes for the SHELF experiment. a) Incoming energy flux
557 calculated from the No TOPO simulation (figure 8a). Note that the shelf bathymetry is
558 contoured on this plot (grey lines, and green “land”), but this bathymetry was not part
559 of this simulation. The green line demarks the region the energy budget in the inset was
560 integrated over. The green diamonds are the location of a synthetic mooring, and the arrow
561 indicates the estimated incoming flux from a plane wave fit over the three moorings of the
562 “Total” simulation (see text). b) Reflected energy flux calculated from the difference between
563 the velocities and displacements of the Total simulation (panel d) and the “Incoming” (panel
564 a). Blue arrow is the outgoing flux from a plane wave fit over the mooring array from the
565 “Total” simulation. c) Energy flux cross terms between the incoming and outgoing waves. d)
566 Total simulation from the SHELF case (figure 8d)

35

- 567 10 Energy partition as in figure 9, taking the ROUND RISE simulation as the incoming wave, and
 568 SHELF/RISE simulation as the total wavefield. 36
- 569 11 Energy partition as in figure 9, taking the RISE simulation as the incoming wave, and REAL
 570 simulation as the total wavefield. 37
- 571 12 a) Energy budget from 80 km by 80 km control volumes along the continental slope from the
 572 REAL simulations. The incoming flux (red) is compared to the reflected (blue) and the cross
 573 terms (purple). b) The reflection co-efficients. The blue line is R_1 , the mode-1 reflectivity in
 574 the 80-km control volumes along slope from the non-linear simulation. The black line is the
 575 mode-1 reflectivity from a linear model (Kelly et al. 2013a), and the grey lines behind are the
 576 cumulative sum of modes 2, to 5 and then all the modes. These do not sum up to one because
 577 the linear model has some “viscosity” that removes some high-mode energy. The dashed lines
 578 are the mean of R_1 from the linear model if a constant average is taken (light blue, dashed),
 579 and if weighted by the diffracted beam strength (purple, dashed). 38
- 580 13 Barotropic to baroclinic conversion for different shelf widths from widest (a) to narrowest (d).
 581 Arrows are barotropic flux vectors. Note how the along-slope barotropic flux is almost entirely
 582 confined to conversion dipoles along slope. 39
- 583 14 Along-slope spectra of across slope velocity (thick lines) for the three narrowest slopes in
 584 figure 13, from velocities on the shallow shelf in these simulations. The thin lines are resonance
 585 curves, formed from the cross-slope equations of motion assuming harmonic motion in time and
 586 along-slope. As along-slope wavenumber is varied resonant modes have a stronger response.
 587 What is plotted is arbitrary units for the three slope geometries. 40
- 588 15 Terms from the energy budget for 40-km wide slope. The incoming and reflected energy fluxes
 589 are computed at $x = 40$ km, and the conversion term integrated from the shelf to $x = 40$ km. 41
- 590 16 Spatial shape of modes picked out from the resonant searching technique (as shown in fig-
 591 ure 14) for the 70, 40 and 20-km wide slopes. 42

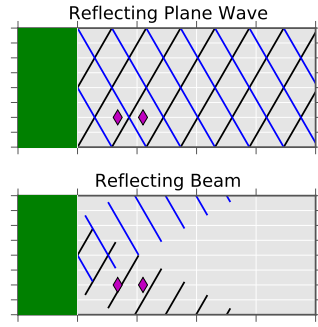


FIG. 1. Schematic of the difficulty of quantifying reflecting fluxes in an inhomogeneous environment. Plane waves are trivial. Inhomogeneous incoming waves or reflections are significantly more difficult.

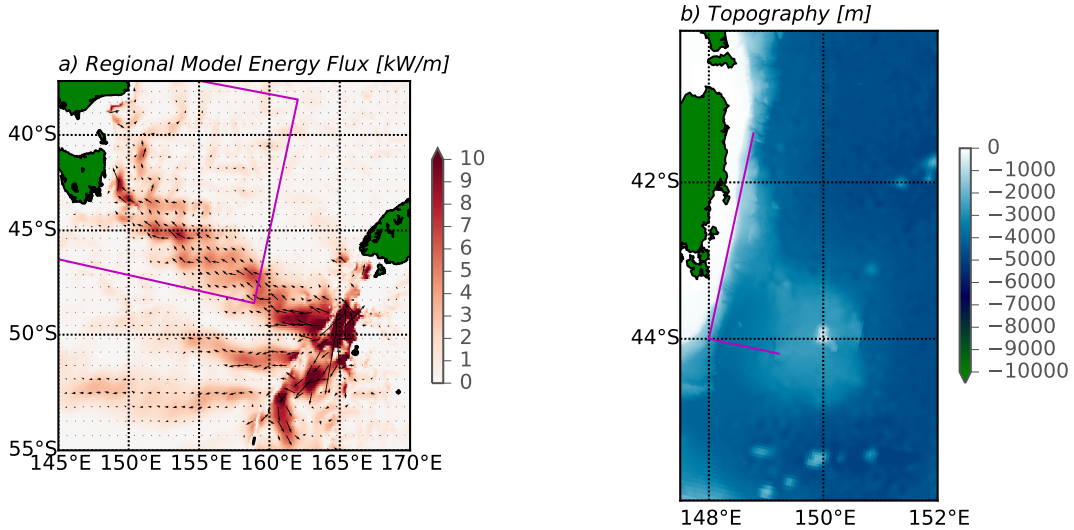


FIG. 2. Location of TTide experiment: a) Energy flux in a regional numerical simulation. Color is the absolute value of the flux, arrows its direction. The magenta box indicates the numerical modeling domain used in this paper. b) Detail of the bathymetry on the Tasman slope. The magenta lines indicate 100 km in the x-direction, and 300 km in the y direction in the modeling domain used in this paper.

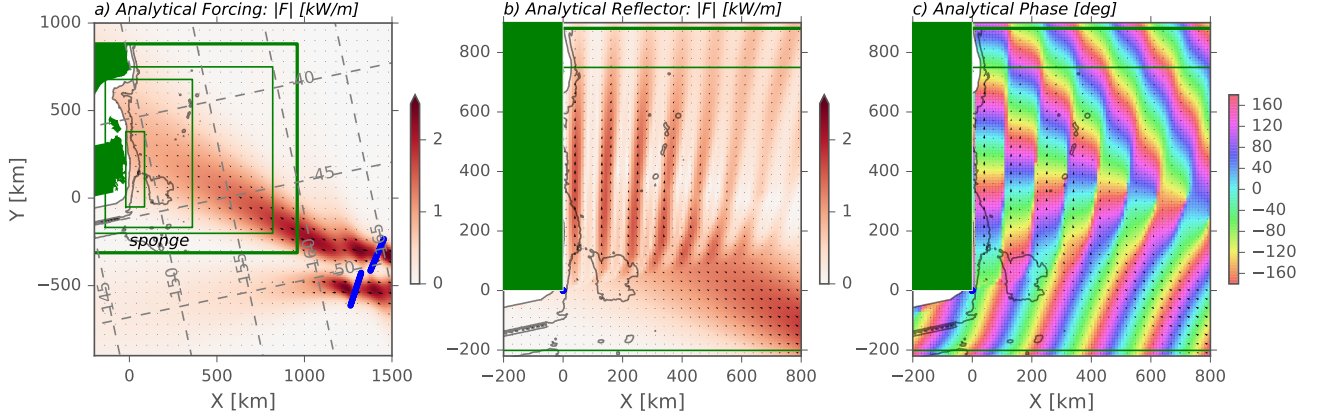


FIG. 3. a) Forcing used to drive the models used in this paper. Two mode-1 internal wave sources are located to the south east (blue lines). The model domain is rotated 12 degrees from geographic so the shelf break approximately lies along $x = 0$. Typical model domain and sponge region is indicated as green rectangles. The 250, and 3000-m isobaths are contoured. Arrows show the direction of the energy flux, and are scaled by its strength. b) Energy flux of analytical response of energy reflecting from a wall at $x = 0$, north of $y = 0$. c) Phase of reflected response.

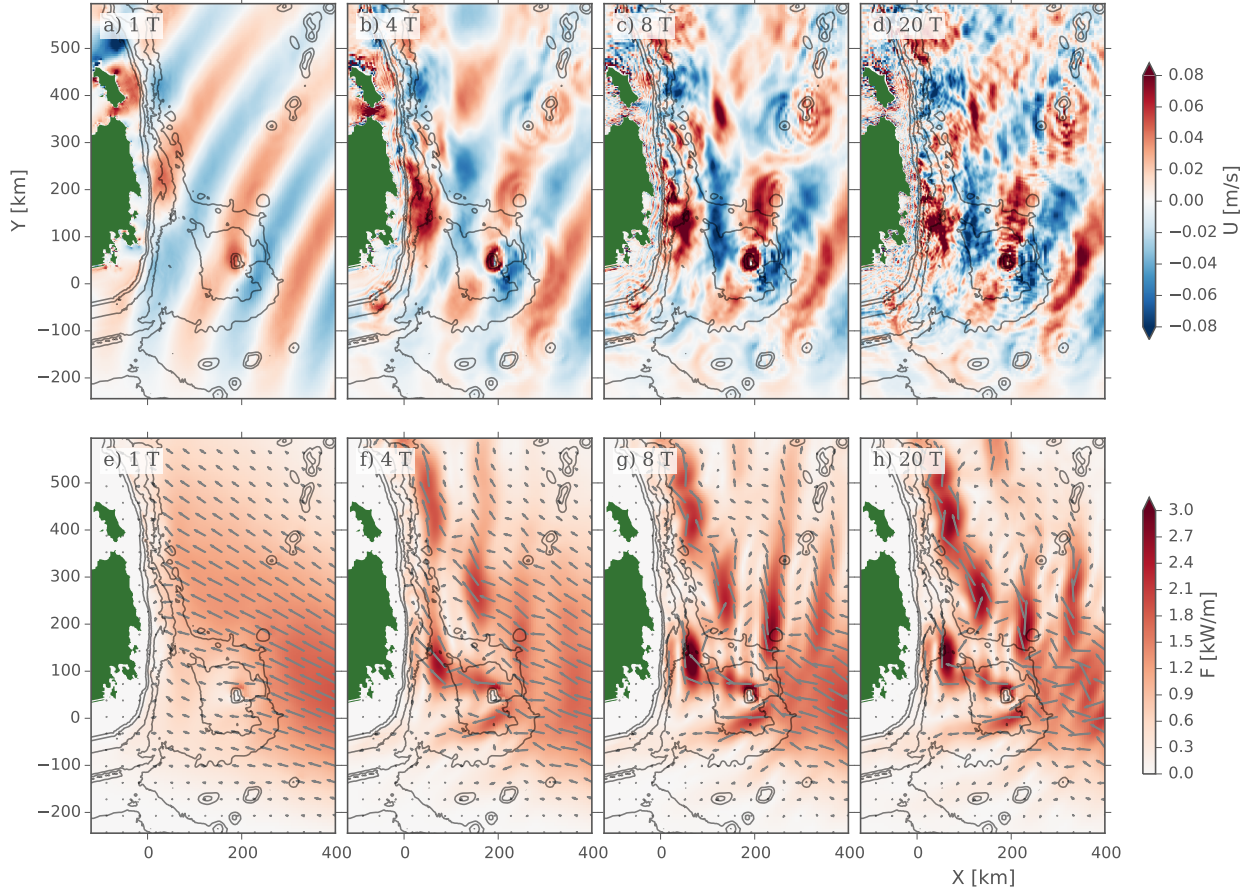


FIG. 4. a)-d) Surface x-direction velocity for four snapshots. a) is the initial conditions (slightly modified after a tidal cycle) and d) is the steady state. Grey contours are depths at 3000, 2000, 1000, and 250-m. e)-h) is depth-integrated baroclinic energy flux at the same time periods, with arrows indicating direction.

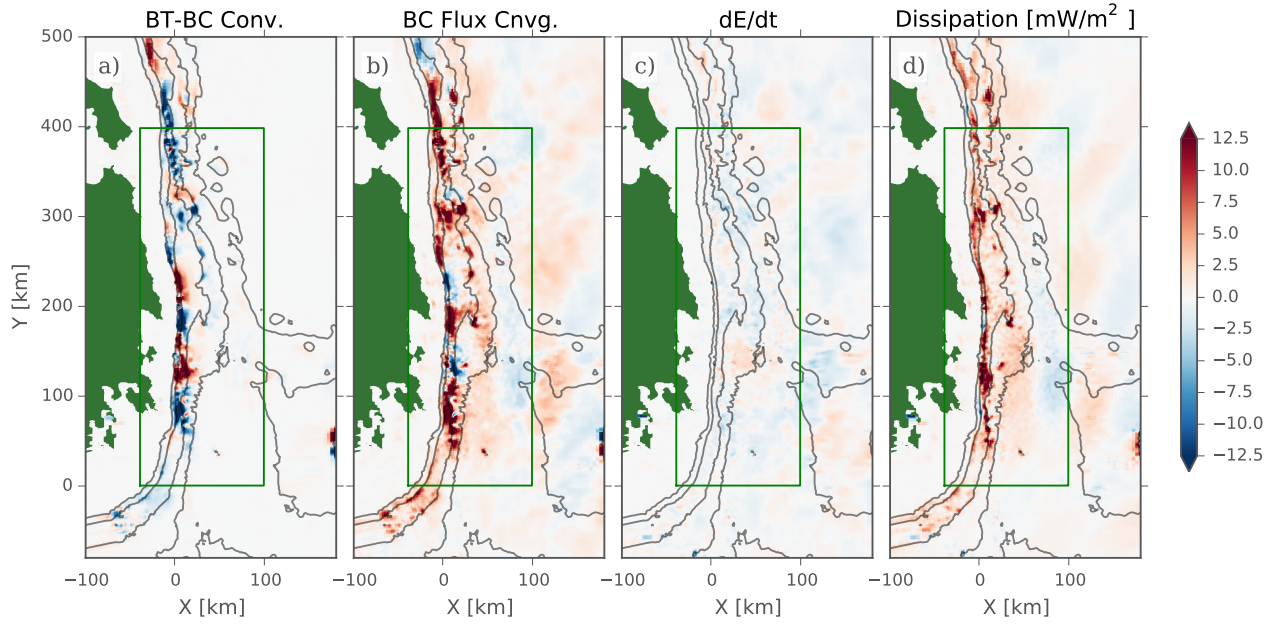


FIG. 5. Energy budget over the 19th tidal cycle of a) Barotropic to baroclinic conversion; b) Baroclinic energy flux convergence ($-\nabla F_{bc}$); c) rate of change of baroclinic energy; d) residual representing the dissipation in the model $D = -\nabla F_{bc} + \text{Conv.} - dE/dt$. The green box is the region for the energy time series (FIG. 6b).

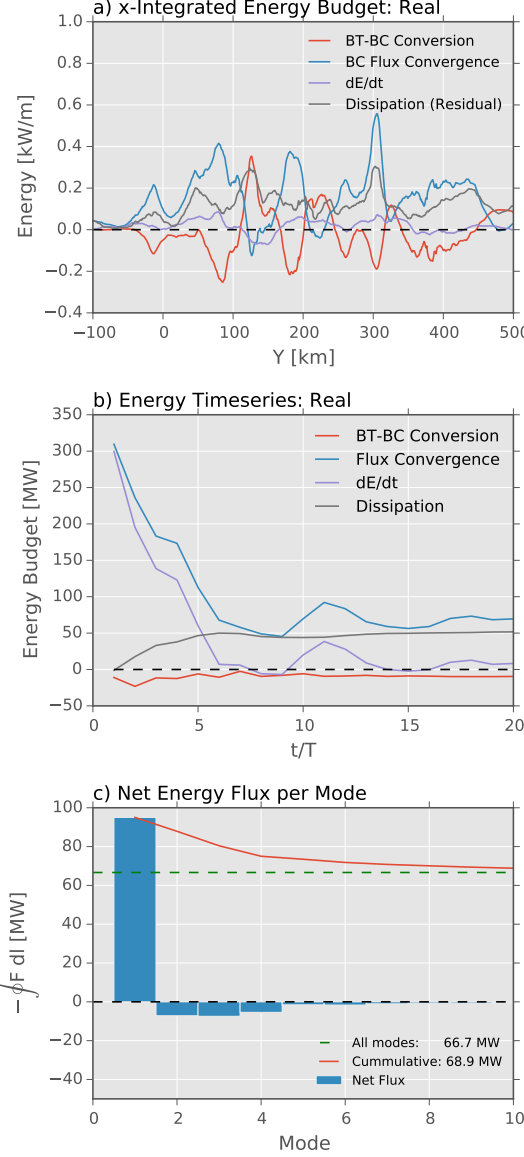


FIG. 6. a) Integral in x to 80 km offshore of the energy terms in FIG. 5 for the REAL case. Note that the barotropic-baroclinic term (red) is of the same order as the baroclinic convergence (cyan) and the residual dissipation (gray) for most of the slope. b) Energy budget time series for the “Real” case, tidally averaged, where time is normalized by $T = 12.4h$, between $y = 0$ to $y = 400$ km. There is still a small residual increase in the energy with time (purple), representing the accumulation of high-mode energy in the region. Net barotropic-baroclinic conversion (red) is small and negative, indicating a small net loss to the barotropic tide in this region. The bulk of the budget is the balance between baroclinic flux convergence (blue) and the residual “dissipation” (gray). c) Net flux in the box defined by $0 < x < 80$ km, and $0 < y < 400$ km. Green is the value for the net flux (no modal decomposition). Blue bars are the modal decomposition. There is a net incoming flux in mode 1 and net reflecting fluxes in higher modes (primarily modes 2-4).

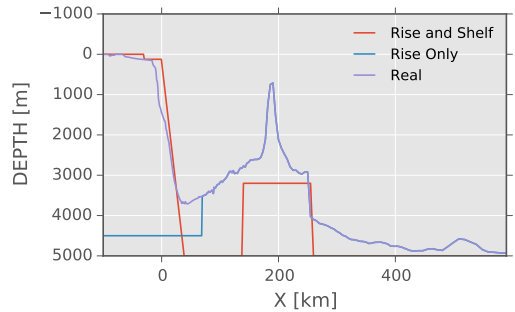


FIG. 7. Cross sections of topographies from $y = 50$ km.

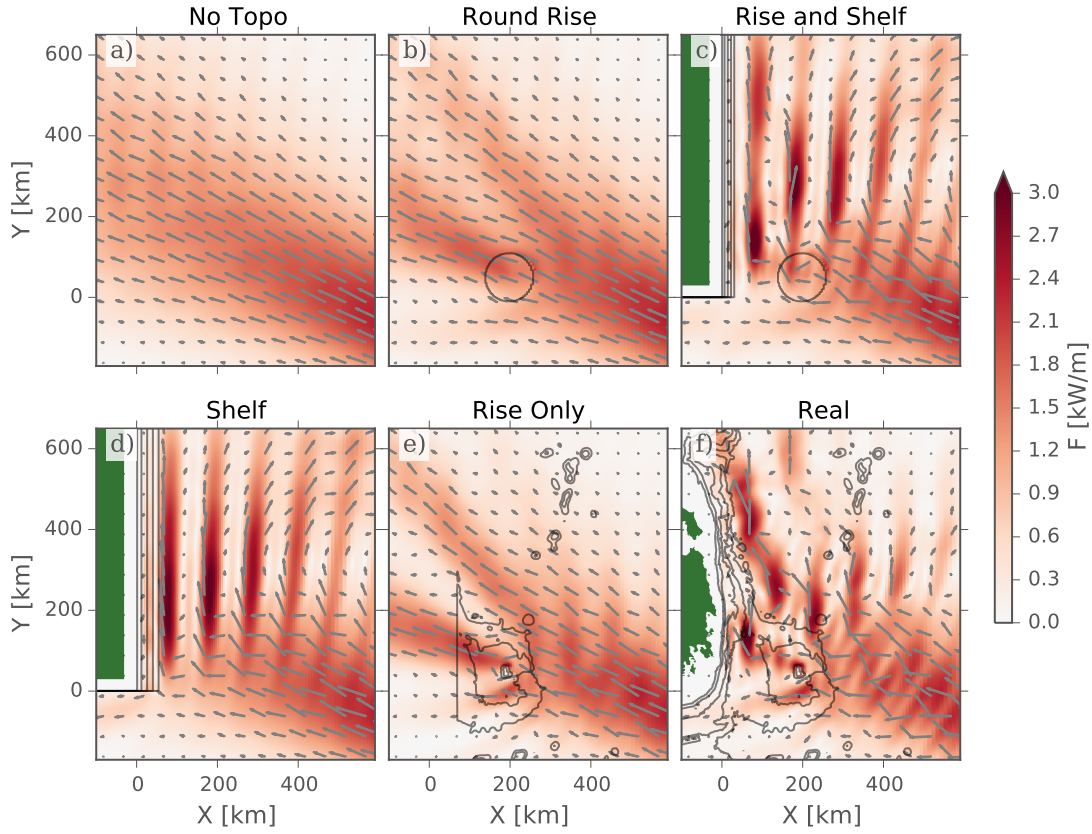


FIG. 8. Energy flux for six geometries at tidal cycle 20. Grey depth contours are -3000, -2000, -1000 and -250 m. Arrows indicate the direction of energy flux. See FIG. 7 for bathymetry cross sections at $y = 50$ km.

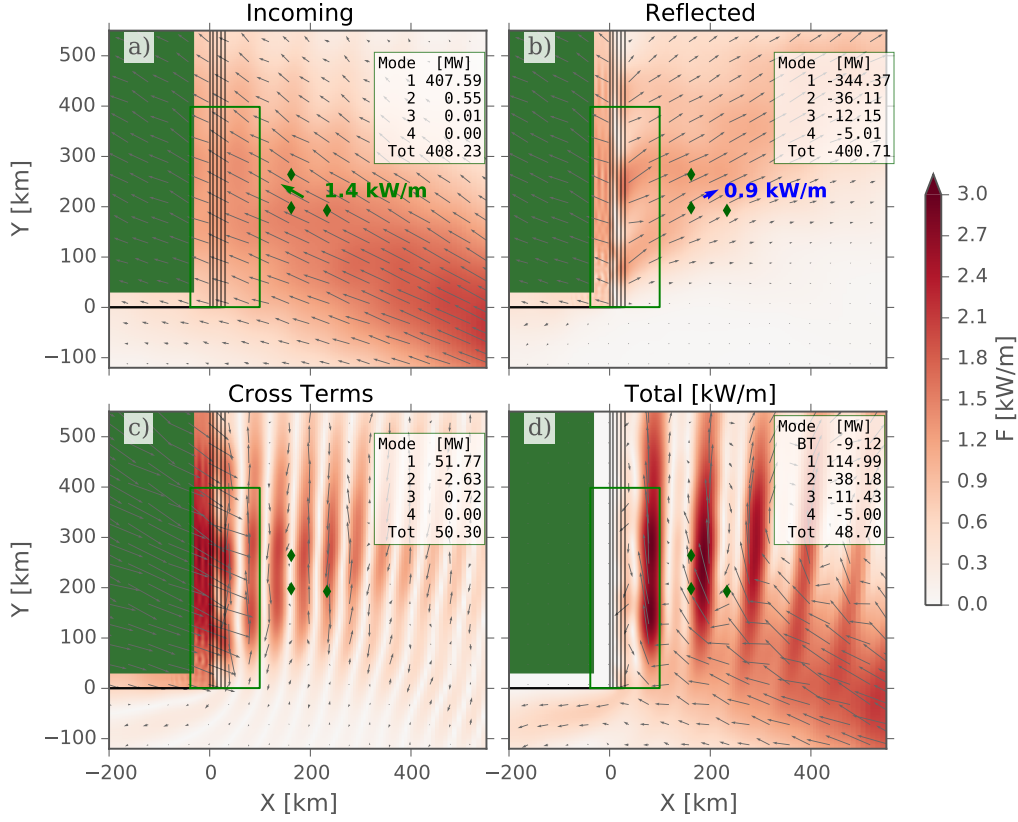


FIG. 9. Mode-1 decomposition of energy fluxes for the SHELF experiment. a) Incoming energy flux calculated from the NO TOPO simulation (FIG. 8a). Note that the shelf bathymetry is contoured on this plot (grey lines, and green “land”), but this bathymetry was not part of this simulation. The green line marks the region the energy budget in the inset was integrated over. The green diamonds are the location of a synthetic mooring, and the arrow indicates the estimated incoming flux from a plane wave fit over the three moorings of the “Total” simulation (see text). b) Reflected energy flux calculated from the difference between the velocities and displacements of the Total simulation (panel d) and the “Incoming” (panel a). Blue arrow is the outgoing flux from a plane wave fit over the mooring array from the “Total” simulation. c) Energy flux cross terms between the incoming and outgoing waves. d) Total simulation from the SHELF case (FIG. 8d)

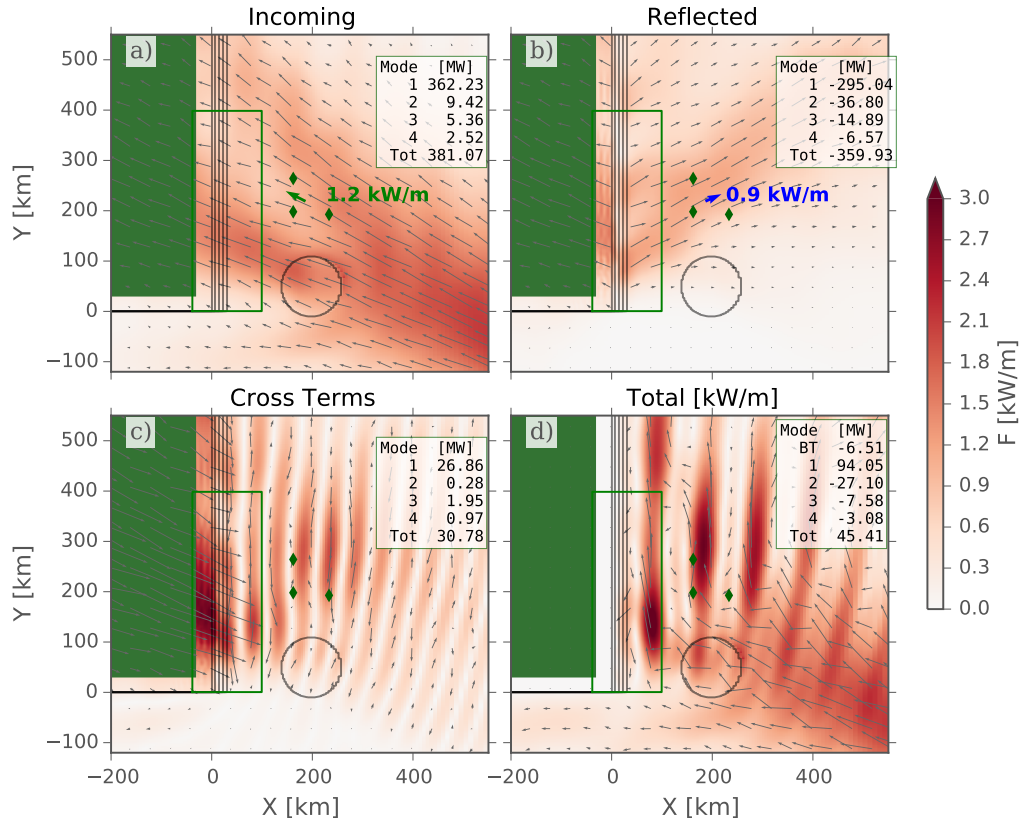


FIG. 10. Energy partition as in FIG. 9, taking the ROUND RISE simulation as the incoming wave, and SHELF/RISE simulation as the total wavefield.

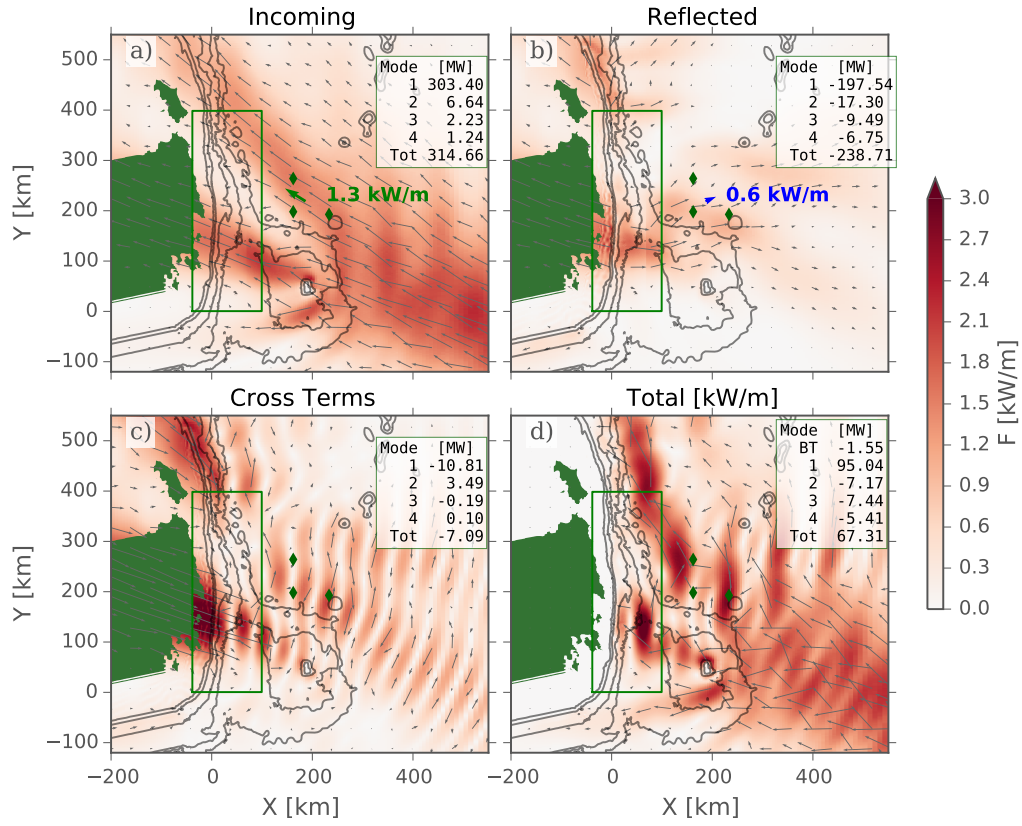


FIG. 11. Energy partition as in FIG. 9, taking the RISE simulation as the incoming wave, and REAL simulation as the total wavefield.

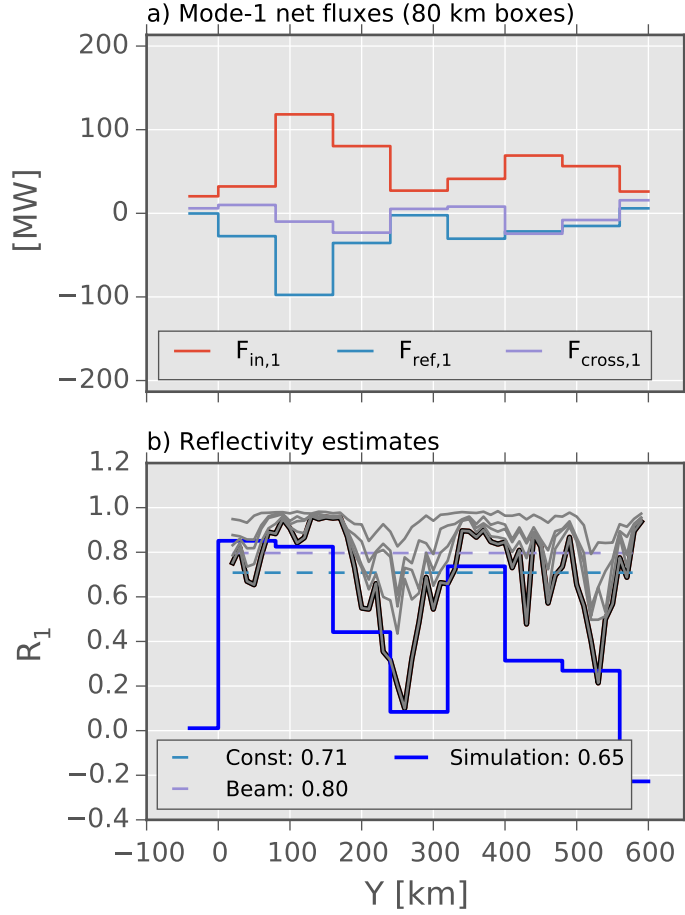


FIG. 12. a) Energy budget from 80 km by 80 km control volumes along the continental slope from the REAL simulations. The incoming flux (red) is compared to the reflected (blue) and the cross terms (purple). b) The reflection co-efficients. The blue line is R_1 , the mode-1 reflectivity in the 80-km control volumes along slope from the non-linear simulation. The black line is the mode-1 reflectivity from a linear model (Kelly et al. 2013a), and the grey lines behind are the cumulative sum of modes 2, to 5 and then all the modes. These do not sum up to one because the linear model has some “viscosity” that removes some high-mode energy. The dashed lines are the mean of R_1 from the linear model if a constant average is taken (light blue, dashed), and if weighted by the diffracted beam strength (purple, dashed).

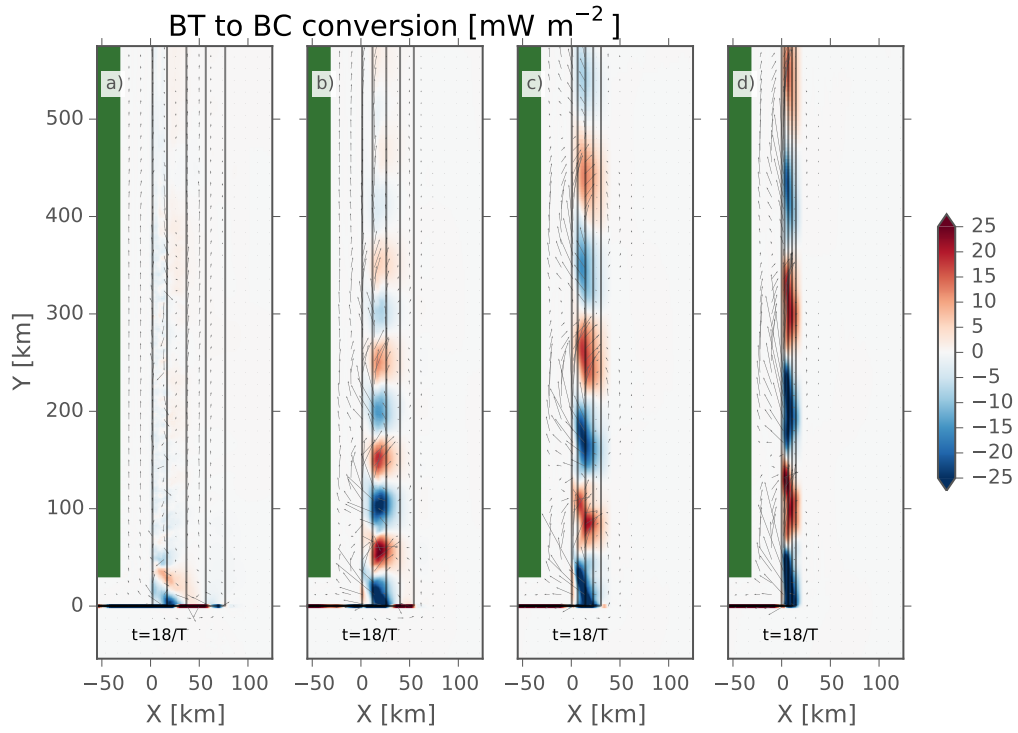


FIG. 13. Barotropic to baroclinic conversion for different shelf widths from widest (a) to narrowest (d). Arrows are barotropic flux vectors. Note how the along-slope barotropic flux is almost entirely confined to conversion dipoles along slope.

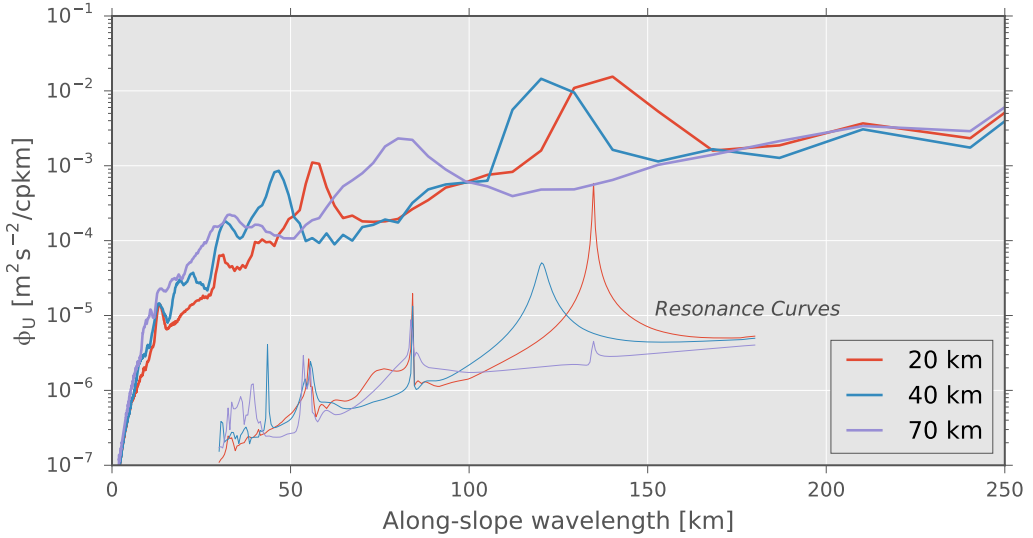


FIG. 14. Along-slope spectra of across slope velocity (thick lines) for the three narrowest slopes in FIG. 13, from velocities on the shallow shelf in these simulations. The thin lines are resonance curves, formed from the cross-slope equations of motion assuming harmonic motion in time and along-slope. As along-slope wavenumber is varied resonant modes have a stronger response. What is plotted is arbitrary units for the three slope geometries.

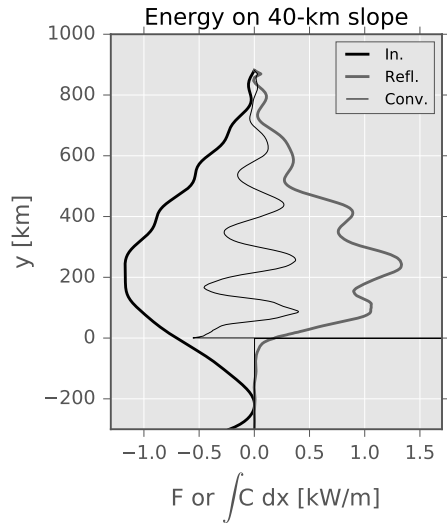


FIG. 15. Terms from the energy budget for 40-km wide slope. The incoming and reflected energy fluxes are computed at $x = 40$ km, and the conversion term integrated from the shelf to $x = 40$ km.

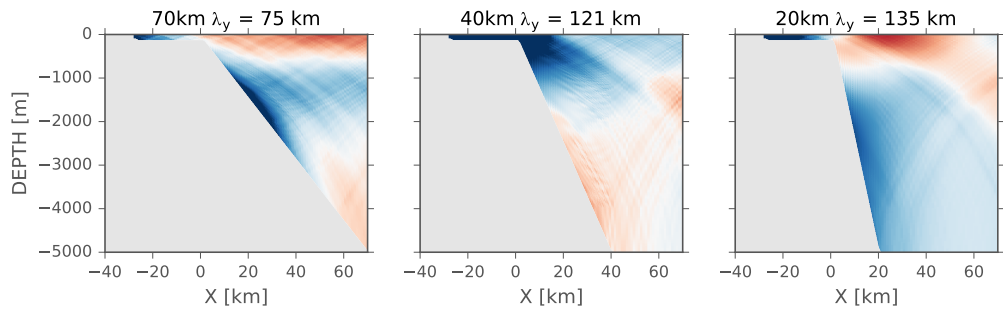


FIG. 16. Spatial shape of modes picked out from the resonant searching technique (as shown in FIG. 14) for the 70, 40 and 20-km wide slopes.